IEEE Access
Multidisciplinary | Rapid Review | Open Access Journal

Received 2 September 2023, accepted 18 September 2023, date of publication 22 September 2023,
date of current version 27 September 2023.

Digital Object Identifier 10.1109/ACCESS.2023.3318481

RESEARCH ARTICLE

Generating Daily Gap-Free MODIS Land Surface Temperature Using the Random Forest Model and Similar Pixels Method

DONG CHEN[1], QIFENG ZHUANG[1], LIANG ZHU[2], WENJIE ZHANG[1], AND TAO SUN[1]
[1]College of Geomatics Science and Technology, Nanjing Tech University, Nanjing 211816, China
[2]Aerospace Information Research Institute, Chinese Academy of Sciences, Beijing 100101, China

Corresponding author: Qifeng Zhuang (zhuangqf@njtech.edu.cn)

This work was supported in part by the National Natural Science Foundation of China under Grant 42301420 and Grant 42271420.

ABSTRACT The land surface temperature (LST) is one of the vital variables for surface-atmosphere interaction. However, due to the vulnerability of thermal infrared remote sensing to clouds, the MODIS LST products have many observation gaps, which seriously limits their application. In this paper, to make up for the shortage of random forest model in reconstructing images with substantial cloud-cover pixels, a combined random forest (RF) and similar pixels (SP) reconstruction scheme was proposed to generate daily gap-free MODIS/Terra LST product and validated by the automatic weather stations (AWS) data in the Heihe River Basin. First, we used the RF model to reconstruct the images that meet the threshold (the clear-sky pixels percentage is more than 30%). Then, we used a combination of the RF model and the SP method to reconstruct the images that do not meet the threshold. Thus, the daily MODIS LST reconstruction results were obtained. The visual assessment indicated that the reconstructed LST strongly correlates with the original LST and can capture the spatial distribution features of LST-related characteristic variables. Additionally, the validation with in situ observations demonstrated that the method of directly using the RF model performs well with an R^2 of 0.87, an NSE of 0.87, an RMSE, and a Bias of 4.69 K and 0.08 K, respectively. The RF model and SP method combination still have a good performance with an R^2 of 0.79, an NSE of 0.76, and an RMSE and Bias of 6.37 K and 0.62 K, respectively.

INDEX TERMS Land surface temperature (LST), remote sensing, MODIS, random forest (RF) regression, reconstruction, similar pixels (SP).

I. INTRODUCTION

Land surface temperature (LST) is one of the most important environmental parameters describing the regional and global land surface-atmospheric interaction and water circulation processes [1], [2]. It is irreplaceable an irreplaceable role in urban heat island effect research, surface energy flux estimation, evapotranspiration research, and soil moisture estimation [3], [4]. The investigation of LST retrieval algorithms has been widely applied in many significant research fields, including climate, ecology, hydrology, and global environmental change [5], [6].

The traditional ground-based measurement sometimes is challenging to meet the requirements of obtaining LST products and their spatial-temporal distribution on regional and global scales. However, in recent years, with the rapid development of remote sensing technology, remote sensing satellite data sets from all over the world have made the rapid acquisition of LST products a reality [7], [8]. Since the 1970s, it has gradually become one of the hotspots in the field of quantitative remote sensing to use the Spaceborne Thermal infrared remote sensing technology to carry out the macroscopic and dynamic temporal and spatial evolution pattern of LST [9]. The relevant satellite data sets include the Moderate Resolution Imaging Spectrometer (MODIS), the Advanced Very High-Resolution Radiometer (AVHRR), and the Advanced Along-Track Scanning Radiometer (AATSR),

The associate editor coordinating the review of this manuscript and approving it for publication was Hongjun Su.

etc. [10]. The MODIS sensors carried on the Terra and Aqua satellites are one of the most widely used sources of satellite-derived LST because of their superior spatial and temporal resolution and long-term availability [11]. MODIS provides multiple daily LST products from thermal infrared bands using the generalized split-window (GSW) algorithm [12]. MODIS LST products have been successfully applied in urban heat island research, surface energy flux estimation, cropland evapotranspiration estimation, etc. [13], [14]. However, thermal infrared remote sensing can still not overcome the interference of clouds and fog. In the case of cloudy weather or other atmospheric interference radiation transmission, it significantly impacts the retrieval of LST [15]. Infrared sensors can detect the heat released from any surface they observe, but they can not penetrate the thick cloud layer. As a result, the existing thermal infrared remote sensing inversion algorithm is only applicable to clear-sky conditions, resulting in a large number of missing surface temperature information under cloud cover conditions and null-value pixels in the LST products appear more or less, which dramatically limits the in-depth application of surface temperature in relevant fields [16], [17], [18]. Therefore, accurate estimation of LST of cloud-covered pixels is an urgent issue to expand the application of LST and promote the research of thermal infrared remote sensing.

Driven by the rapid development of earth observation technology, the reconstruction methods for cloud-covered pixels can be separated into three categories: spatial-based, temporal-based, and spatiotemporal-based [19]. For spatial-based methods, the invalid pixel mainly determines the objective function through the spatial relationship between its adjacent pixels. It restores the invalid value, which is the most widely used, including inverse distance weighting, the Kriging method, Co-Kriging, and adjusted Kriging [20], [21]. For temporal-based methods, invalid pixels are reconstructed by time information between different pixels on the same timeline without considering the values of geographically adjacent pixels. Based on this idea, Arroyo and Villajos [22] and Zhang et al. [23] proposed the Linear Temporal method. The change law of LST in 8 days before and after the target pixel is analyzed, and the linear equation is determined, which can be applied to fill invalid values using temporal information. Yan et al. [24] and Yang et al. [25] used the Savitzky-Golay (S-G) method and the Harmonic Analysis of Time Series (HANTS) to interpolate daily invalid data, respectively. The spatiotemporal-based methods consider neighboring pixels in both the temporal and spatial domains. Zeng et al. [15] established an adaptive window with invalid pixels as the center to search for effective and similar pixels (SP) geographically and combined the effective information of images on adjacent days to accomplish the search process. The best estimate for the clear-sky equivalent LST was proposed by Chen et al. using multiple temporally adjacent images as reference [26]. Additionally, Yu et al. [27], Tan et al. [28], and Chen et al. [29] assumed that adjacent pixels in the temporal and spatial domains are similar pixels (SP) with high correlation. This method was used to construct a transfer function between SP to recover LST under cloudy conditions. Previous research shows that the SP method is a highly explanatory and practical interpolation.

In addition to the above methods, with the development of machine learning algorithms in recent years, some reconstruction methods based on artificial neural networks, random forest, and support vector machines have gradually emerged [30], [31]. Wu et al. reconstructed the gap-free LST of Wuhan City from 2016 to 2021 using a random forest model that considers spatial characteristics [32]. Recurrent neural network (RNN) and short-term memory (LSTM) neural network models also exhibit typical performance in temperature reconstruction [33], [34]. Chung et al. constructed a air temperature estimation LSTM model using different LST data during cold and hot periods in one year and achieved acceptable performance during cold periods [35]. Yang et al. also evaluated the performance of large-scale LSTM models for air temperature [36]. Artificial neural networks (ANN) also have very broad application prospects in temperature reconstruction [37], [38]. Wang et al. used the ANN model to accurately reconstruct air temperature in complex mountainous areas [39]. Sahin used the ANN model to model the monthly average temperature of 20 cities [40]. Wu et al. developed a multi-scale feature connection model using convolutional neural networks (CNN) to reconstruct LST datasets with large missing regions [41]. LST is greatly affected by solar radiation, land use type, vegetation cover, terrain, etc. [42], and LST has substantial space and heterogeneity. The machine learning method, with its simple, fast, no complex physical mechanism, considering the surface spatial heterogeneity, can establish an ideal relationship between LST and related impact factors and has a broad application prospect [41]. Therefore, the results obtained by machine learning-based methods are often highly +accurate and suitable for more accurate LST reconstruction. The RF model is a classic machine learning model for LST reconstruction, as it reduces the risk of overfitting by combining multiple weak classifiers to form a robust classifier. Zhao and Duan [43] reconstructed the MODIS/Terra LST data using European second-generation geostationary meteorological Meteosat Second Generation (MSG) solar radiation data and other surface variables (vegetation index, surface albedo, water index, and topographic characteristics). The random forest (RF) algorithm was used to construct the correlation model under the clear-sky pixel element, and the association model was applied to the cloud coverage pixel area. The real surface temperature of the cloud cover element was reconstructed with high accuracy. Li et al. used various machine learning methods to reconstruct LST, including ANN, SVM, and RF. The results indicate that RF performs better than other methods [44]. As a machine learning method, RF can connect LST with its most relevant influence variables and construct a fitting function, and the training process is

relatively straightforward [45]. However, when using RF to carry out the LST reconstruction work, the reconstruction accuracy is affected by the number and numerical distribution of training sample sets to a certain extent. The relationship between related impact factors and reconstruction results is still worth discussing. In addition, in previous studies on LST reconstruction using the RF model, there is still no good solution for images with severe cloud pollution and almost no clear-sky pixels. Xiao et al. only reconstructed images with clear sky pixels that meet a certain threshold within a year using the random forest model [46].

Hence, to address the limitations of the RF model in reconstructing heavily polluted images, we proposed an improved LST reconstruction scheme using the RF model and SP method to generate daily gap-free MODIS/Terra LST product. We selected the Heihe River Basin (HRB) as the study area and reconstructed the daily MODIS/Terra LST product in this area in 2019. The reconstruction results were validated by in situ observations from automatic weather stations (AWS) [47], [48] and the relationship between the accuracy of the reconstruction results and the training samples was quantitatively evaluated.

II. MATERIALS

We introduced daily auto weather station data with parameters for geography and time, remotely sensed data and other ancillary data to conduct our work. All data and their abbreviations used in this study are listed in Table 1.

TABLE 1. Variables used for the RF model estimation in 2019.

Data Sources	Abbreviation	Data	Spatial Resolution	Temporal Resolution
AWS	LST	Land surface temperature	/	30 min
MODIS	NDVI	Normalized difference vegetation index	500 m	Daily
	EVI	Enhanced Vegetation Index	500 m	Daily
	MNDWI	Modified Normalized Difference Water Index	500 m	Daily
	LSWI	Land surface water index	500 m	Daily
	LST	Land surface temperature	1000 m	Daily
SRTM	DEM	Digital Elevation Model	90 m	/
	SLP	Slope	90 m	/
TPDC	SWDR	Short-wave downward radiation	0.05°	10 min

A. AWS MEASUREMENTS

The in situ LST measurements from AWS thermal infrared thermometer observation validated the reconstructed LST. The average frequency of AWS observation results is half an hour. The validation data of four auto weather stations in 2019 were used in this study: Arou (AR), Dashalong (DSL), Sidaoqiao (SDQ), and Zhangye (ZY) [47], [48]. Detailed information on these eight locations is shown in Table 1.

TABLE 2. Site location and underlying surface information of Heihe River Basin.

Sites	Land Cover	Longitude(E)	Latitude(N)	Elevation(m)
AR	Alpine meadow	100.4643	38.0473	3033
DSL	Swamp meadow	98.9406	38.8399	3739
ZY	Wetland	100.4464	38.9751	1460
SDQ	Tamarix	101.1374	42.0012	873

B. MODIS PRODUCTS

In this study, the 1 km MOD11A1 product was selected to complete the reconstruction of MODIS/Terra LST. According to the quality assurance description from the MODIS quality control (QC) band, we set the part that does not generate LST due to cloud effect and the portion that does not cause LST due to reasons other than cloud effect the LST that needs to be reconstructed.

The surface reflectance data was selected from MOD09GA in this study. NDVI, EVI, and MNDWI were calculated based on different reflectance bands. NDVI was calculated with the red and near-infrared bands' reflectance, MNDWI was calculated with the green and mid-infrared bands' reflectance, and EVI was calculated with the red, blue, and near-infrared bands' reflectance. LSWI was calculated with the near-infrared and the shortwave infrared bands' reflectance. All the MODIS datasets are downloaded from NASA's Earthdata website (https://appeears.earthdatacloud.nasa.gov/, accessed on 23 July 2022) for free.

C. TOPOGRAPHIC DATA

The elevation and slope data used in this study were obtained free from Shuttle Radar Topography Mission (SRTM) 90-m DEM data (http://srtm.csi.cgiar.org/, accessed on 31 July 2022). According to the DEM data, elevation and slope data were calculated to be the terrain factors in the reconstruction process. Using the bilinear interpolation method, they were resampled into 1 km to keep consistent with the MODIS LST data.

D. SOLAR RADIATION DATA

Surface downward shortwave radiation is the primary energy driving surface temperature changes; accurately obtain the difference in radiation conditions caused by surface cloud coverage, the East Asia-Pacific longwave/shortwave downward radiation at the surface data set (2016-2020) was applied in this study (http://data.tpdc.ac.cn/, accessed on 13 August 2022) [49]. The temporal resolution of the shortwave radiation data is 10 minutes, and the spatial resolution

is 5 km respectively. The product is developed by the geostationary satellite Himawari-8, which can provide radiation estimates under the clear-sky pixels and cloud-cover pixels and have higher spatiotemporal resolution than other radiation products such as the fifth generation ECMWF atmospheric reanalysis of the global climate data (ERA5) and The Global Land Surface Satellite (GLASS) product. To fully consider the cumulative effect of radiation factors on the surface temperature, V_{SOL} represents the cumulative value of surface solar radiation from sunrise to satellite observing time (10:30 am). V_{SOL} value was estimated by integrating all instantaneous data within the time range and resampled into 1 km to keep consistent with the MODIS LST data.

III. METHODOLOGY

A. STUDY AREA

The Heihe River Basin (HRB) is located between 97.1° E to 102.0° E and 37.7° N to 42.7° N, which is the second largest inland river in the arid region of northwest China, flowing through Qinghai Province, Gansu Province, and Inner Mongolia Autonomous Region. HRB is rich in underlying surface types, characterized by alpine and arid and semi-arid landscapes, mainly grassland and green coniferous forest; in the middle reaches, primarily corn, wheat, and other crops; in the lower reaches, mainly riverbank mixed forest.

The terrain of the HRB is high in the south, low in the north, high in the West, and low in the East. Qilian Mountain in the South has the most considerable altitude change and is the basin's primary source of snowmelt water. The annual average temperature, rainfall, and evaporation potential in the study area are 7.5° C, 136.8 mm, and 1840.1 mm, respectively. The arid region and the cold area coexist in the river basin, with extremely distinct climatic characteristics, making the HRB an ideal experimental river basin for the comprehensive study of the river basin. Rich surface types create different ecological landscapes, which can also thoroughly test the reconstruction performance. The international Geosphere-Biosphere Program (IGBP) classification was employed to distinguish the different land surface types. Fig. 1 shows the detailed introduction of the HRB.

B. RANDOM FOREST MODEL

This study used the Random Forest algorithm to construct the LST reconstruction model. For the same surface, the difference between LST under clear-sky and cloudy-sky conditions is mainly due to the difference in surface solar incident radiation caused by cloud cover. Therefore, the actual LST of each pixel is directly related to the cumulative radiation received by the pixel. To quantitatively express the effect of environmental factors on LST, Zhao and Duan [43] proposed an RF-based model to reconstruct LST under cloudy conditions. The cumulative solar radiation information of each pixel was extracted through MSG data. The empirical surface temperature estimation model was established together with characteristic variables (Normalized Difference Vegetation Index (NDVI), Enhanced Vegetation Index (EVI), Normalized Difference Water Index (NDWI), surface albedo, elevation, slope, and latitude) to characterize the nonlinear relationship between LST and radiation and local surface parameters. The estimation model was applied to the pixels under cloudy conditions to realize the LST reconstruction of this pixel. Mokhtari et al. believe that Land Surface Water Index (LSWI) is a parameter highly related to LST [50].

On the other hand, surface albedo is also vulnerable to cloud cover. Hence, in this study, characteristic variables were chosen as NDVI (V_{NDVI}), EVI (V_{EVI}), MNDWI (V_{MNDWI}), LSWI (V_{LSWI}), elevation (V_{ELV}), slope (V_{SLP}), latitude (V_{LAT}), and solar radiation factor (V_{SOL}). Modified Normalized Difference Water Index (MNDWI) was used instead of NDWI. The RF-based model was firstly used to establish the LST linking model with the characteristic variables under clear-sky conditions. The model was trained

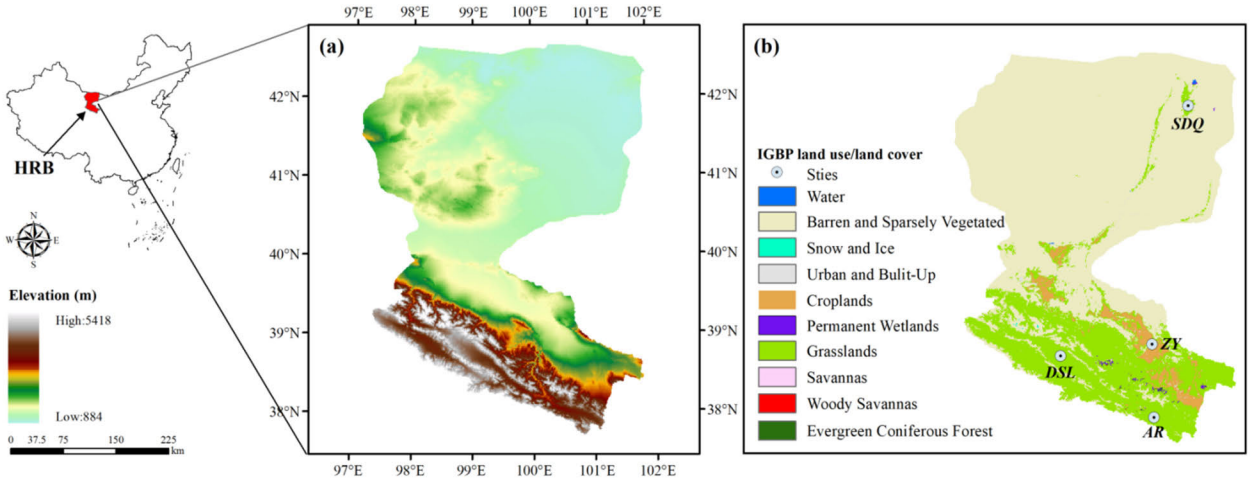

FIGURE 1. (a) The location of the study area and the distribution of elevation. (b) IGBP land use type and site location in the study area.

based on the effective LST and its characteristic variables under clear-sky conditions. Then, the perfectly trained LST linking model was applied to the pixels covered by the cloud, and the actual LST value was estimated by combining the corresponding characteristic variables.

C. SIMILAR PIXELS METHOD CONSIDERING THRESHOLD

During the estimation process, the number of pixels under clear-sky conditions used to train the LST linking model should be large enough to accurately capture the relationship between the LST and its characteristic variables. Gu et al. believed that the training set with low correlation inevitably reduced the accuracy of the random forest model [51]. For some images with severe cloud pollution and few clear-sky pixels, it is unreasonable to use the random forest model to predict LST. Therefore, we set a 30% threshold for the effective pixels percentage of LST which participate in the LST linking model training. If the clear-sky pixels percentage of the LST product is less than 30% on a specific day, the LST product on that day will not be reconstructed. This is the result obtained after multiple tests. As shown in Fig. 2, in 2019, the number of days meeting the above requirements is 290, and the number of days needing recovering the invalid value through temporal reconstruction is 75. However, it is still challenging for the random forest model to reconstruct images with almost no adequate information. Therefore, to generate daily MODIS/Terra LST product, based on the SP method used by Yu et al. [27] and Tan et al. [28], we proposed an RF and SP-based reconstruction method for LST images whose effective pixels percentage does not meet the threshold. The common point is to complete the reconstruction of invalid values by searching for similar pixels related to invalid pixels and establishing the relationship between them. The specific method is that for each LST image whose clear-sky pixels percentage does not meet the threshold, the LST image whose clear-sky pixels percentage meets the threshold closest to it in time was searched. The LST linking model was trained by combining the clear-sky pixels of the two images.

Then, the trained LST linking model was used to recover LST products whose effective pixels percentage did not meet the threshold. As shown in Figure 3, we combine the RF model with the SP method to propose a new LST reconstruction scheme. the RF model divides the input dataset into a training dataset and a testing dataset, accounting for 66.7% and 33.3% respectively. The training process is divided into two steps. Firstly, LSTs that meet the threshold within a year are placed in the RF model for training, and the reconstruction results that meet the threshold are obtained; Then, LSTs that do not meet the threshold within a year are combined with similar pixels searched by the SP method and trained in the RF model to obtain reconstruction results that do not meet the threshold. By integrating the reconstruction results of the two parts, the daily gap-free LST can be obtained. Before training the model, two meta-parameters should be adjusted to obtain the optimal RF model: the number of decision trees in the forest (ntree) and the number of predictor variables randomly selected on each node of the trees (ntry). According to Belgiu and Drăguţ [52], the ntree and ntry values were set as 500 and 2, respectively. This study used the Python machine learning library (Scikit-Learn) to construct the reconstruction model. ntree and ntry correspond to n_elements and max_features in the Python Random Forest algorithm. The decision tree maximum depth (max_depth) was not restricted.

IV. RESULTS

A. ASSESSMENT OF ORIGINAL LST AND CHARACTERISTIC VARIABLES

1) ORIGINAL LST

The visual assessment of the original LST can intuitively feel the data missing from MODIS/Terra LST product. To better show the reconstruction effect of random forests, we randomly selected four days of the year to analyze the temporal and spatial distribution of LST in the Heihe River Basin. These days are in four different seasons (the day of the year (DOY) 20, 86, 232, 298 in 2019), respectively. In terms of temporal scale, DOY 20, DOY 86, DOY 232, and DOY 298 represented the winter, spring, summer, and autumn in a year, respectively. The data missing in these four days is severe, and their effective pixel percentages

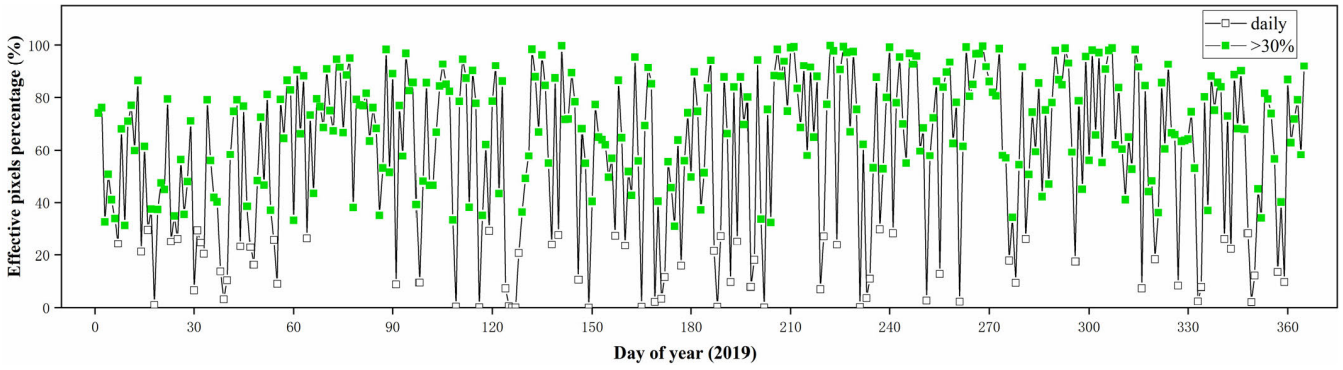

FIGURE 2. Percentage of daily MODIS/Terra LST clear-sky pixels in 2019 and their changes.

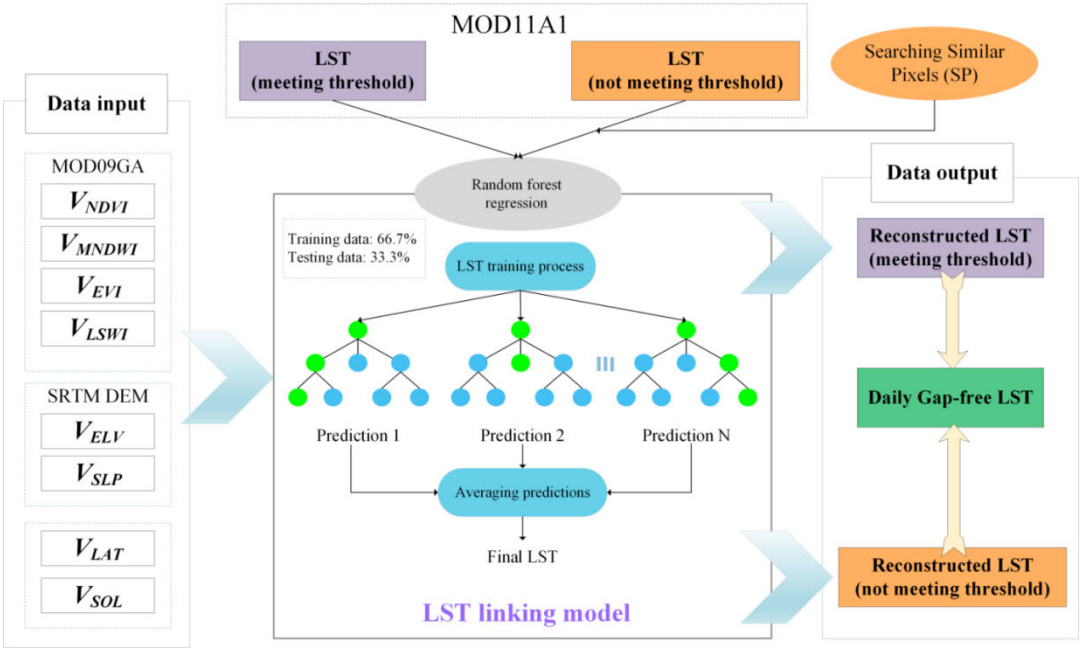

FIGURE 3. Flowchart of daily gap-fee LST reconstruction based on random forest model and similar pixels method.

are 47.41%, 35.17%, 62.30%, and 45.00%, respectively. Subsequent reconstruction results verification will also be based on these four days. The spatial distribution of clear-sky LST pixels on these four days is shown in Fig. 4. In terms of spatial scale, the spatial distribution of clear-sky LST pixels in these four days is different.

On the whole, they are distributed in middle and high latitudes and a few in low latitudes. The upper reaches of the HRB, an area located near Qilian Mountain, with a high altitude and are easily covered by clouds. The middle and lower reaches of the HRB are arid area dominated by desert, with a low altitude, and is often exposed to direct sunlight for a long time. The significant difference in LST in these four days can represent the distribution characteristics of LST in the whole basin within one year. Fig. 5 shows the histogram of characteristic variables (LST, NDVI, and elevation) in these four days. As input data of the random forest model, the distribution of clear-sky pixels often showed significant differences and featured a large value range. The difference in elevation and NDVI represented differences in air temperature and vegetation cover, respectively. These are the factors that directly affect LST. On the other hand, different spatial distribution results in distinct spatial correlation, input data with significant differences can help the random forest model capture the characteristics of the prediction variables and deduce the relationship between LST and characteristic variables. This played a vital role in promoting the training of the random forest model and obtaining better accuracy.

2) THE IMPACT OF THE CLOUD ON MODIS LST PRODUCTS

Solar radiation information can reflect the degree of cloud cover in a region. The solar radiation factor V_{SOL} used in this study was estimated from the accumulated surface solar radiation from sunrise to satellite observing time. Fig. 6 shows the Spatial distribution of cumulative solar radiation and LSWI in 2019. V_{SOL} can reflect the influence of cloud cover on solar radiation in warming the surface. For areas with severe cloud cover, the value of V_{SOL} should be meager.

Similarly, the cloud will also have an impact on LSWI. The aggregation of clouds will increase the LSWI value. By comparing Fig. 4 and Fig. 6, it can be seen that the clear-sky pixels have similar spatial distribution characteristics with the high-value pixels of V_{SOL}. On the other hand, the clear-sky pixels also have identical spatial distribution characteristics with the low-value pixels of LSWI. Therefore, this study's solar shortwave radiation products can effectively monitor solar radiation under different conditions. Based on this, the random forest model can accurately capture the relationship between LST and other characteristic variables, especially the impact of cloud cover.

3) VALIDATION OF RECONSTRUCTION LST BASED ON CLEAR-SKY PIXELS

To validate the result of the RF reconstruction, the density scatter plots between the reconstructed LST by RF and the original MODIS clear-sky pixels are shown in Fig. 7. Overall, the good validation results show excellent random forest model fitting performance. The coefficient of determination (R^2) is above 0.96, and the root mean squared error (RMSE) is lower than 1 K. This shows that the RF model maintains relative stability in different seasons. The reconstructed LST is consistent with the original clear-sky LST. For the amount of data involved in RF training, the data volume of the four seasons from small to large is

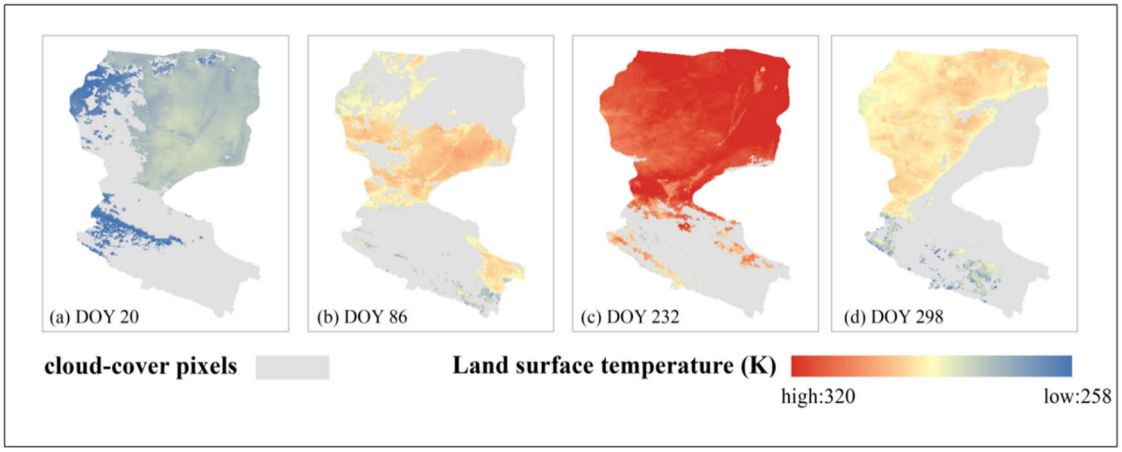

FIGURE 4. The spatial distribution of original MODIS/Terra LST on four days in 2019 (DOY 20, DOY 86, DOY 232, and DOY 298).

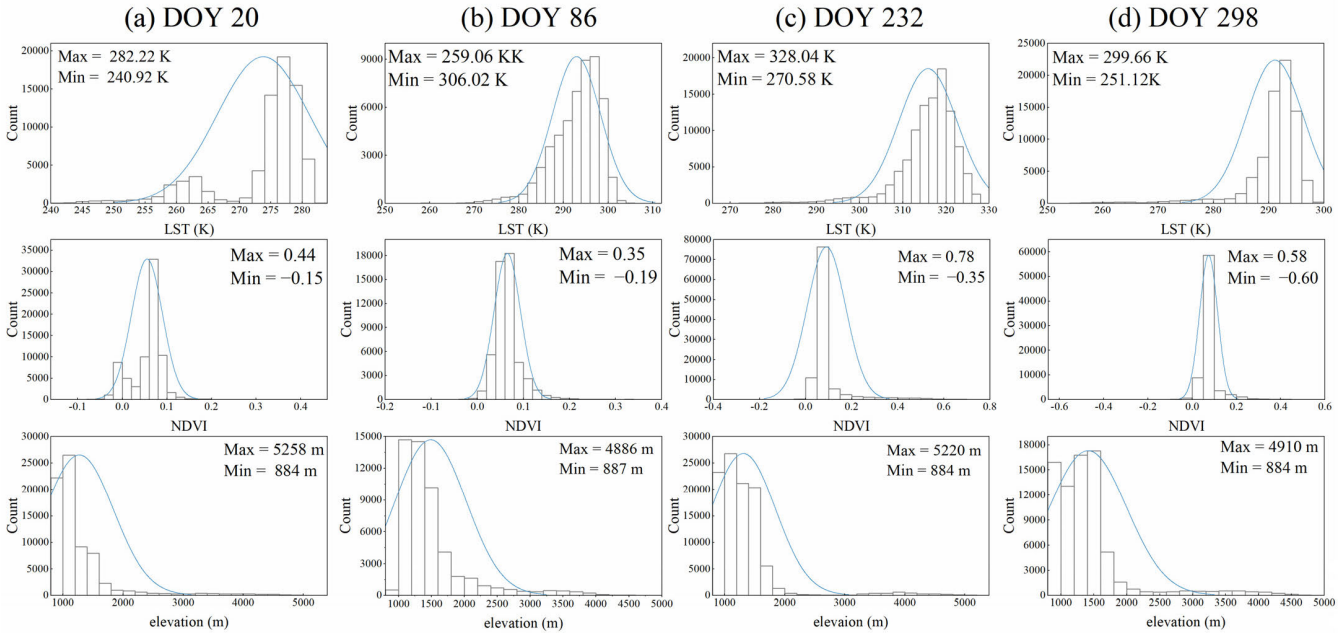

FIGURE 5. Histogram profiles of LST, NDVI, and elevation on four days in 2019 (DOY 20, DOY 86, DOY 232, and DOY 298).

DOY 86 (35.17%), DOY 298 (45.00%), DOY 20 (47.41%), and DOY 232 (62.30%). It is evident that R^2 increases with the increase in data volume. At the same time, RMSE also decreases with the increase in data volume. Although DOY 232 did not show this feature, its RMSE was also within a relatively reasonable range. By contrast, the amount of training data affects the reconstruction accuracy to a certain extent. The more data, the higher the accuracy. During the training process, the RF model randomly divides the input data set into the training and testing parts, containing 66.7% and 33.3% of the data set. The average out-of-bag score of 0.96 also shows that the random forest model can capture the interaction between LST and its characteristic variables well. Different characteristic variables have various contributions to the model. Table 2 shows the average importance score of each characteristic variable on the reconstruction day. The higher the score, the higher the correlation with LST during training. Zeng et al. [15] believe that elevation is an important parameter that cannot be ignored in the LST reconstruction. It can be seen that the characteristic variables with high scores are V_{ELV} (0.35), V_{LSWI} (0.19), V_{LAT} (0.19), and V_{MNDWI}(0.17), respectively.

Among them, V_{ELV} becomes the most relevant characteristic variable of LST. It also shows that elevation has become the most critical factor affecting LST reconstruction in the Heihe River basin, a region with complex terrain and colossal altitude difference. Fig. 8 shows the spatial distribution of LST reconstructed by RF. Compared with the original LST,

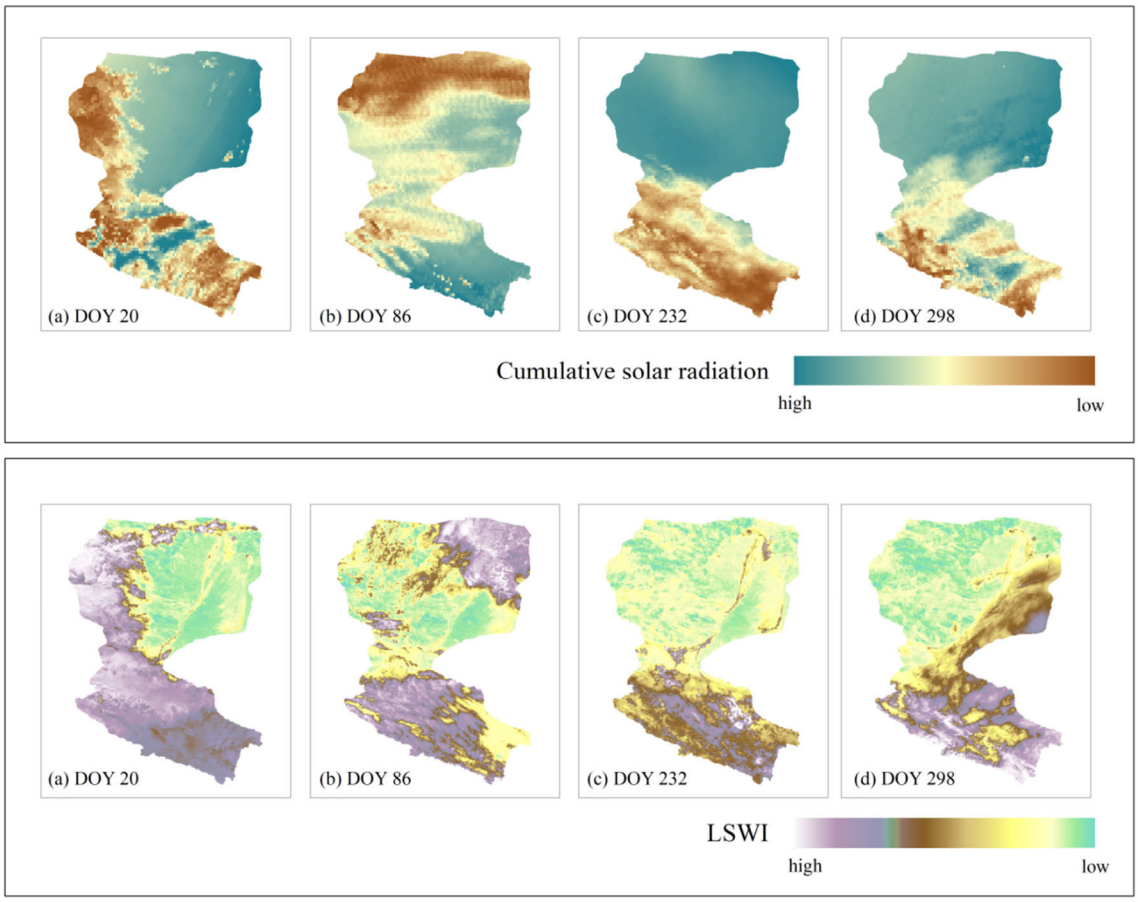

FIGURE 6. Spatial distribution of cumulative solar radiation and LSWI in 2019 (DOY 20, DOY 86, DOY 232, and DOY 298).

the reconstructed LST still has strong spatial similarity. However, the value of recovered LST is lower than the surrounding value of clear-sky pixels. This may be due to the cloud cover, and solar radiation is absorbed or reflected, resulting in the actual surface temperature being lower than the clear sky surface temperature. LST changes related to elevation and latitude can be seen in the images of these four days. Overall, the altitude in low-latitude areas is high, and the LST is usually low; In high-latitude regions, the altitude is low, and the LST is relatively high. Therefore, the RF model can clearly show the spatial distribution characteristics of recovered LST.

B. VALIDATION OF RECONSTRUCTED LST BASED ON IN-SITU LST

1) VALIDATION OF RECONSTRUCTION RESULTS THAT MEET THE THRESHOLD

Ground measurement validation is essential for confirming the accuracy and applicability of LST reconstruction methods. The surface temperature observation data used in this study are from the AWS in the Heihe River basin [47], [48], and the reconstruction results were validated. In 2019, 290 images met the threshold, and these images that met the threshold were directly reconstructed using the random forest model. Fig. 9 shows the reconstructed LST directly using the RF model versus in situ LST of four sites. The scatter plot generally demonstrates that the reconstructed LST using the RF model has a good correlation with in situ LST with an R^2 value of 0.87, the Bias of 0.08 K, and an RMSE of 4.69 K. Most points are densely distributed near the 1:1 line, which indicates that the reconstruction accuracy can reach a satisfactory level. In addition, the value of Nash-Sutcliffe Efficiency (NSE) comes to 0.87, demonstrating that the RF model is compelling and convincing in reconstructing LST.

To better analyze the reconstruction effect of the RF model at different sites, we compared the reconstruction effect of each site. Table 3 shows the validation statistics of these sites. In general, these four sites have performed well in LST reconstruction, and the R^2 varies from 0.79 to 0.92, and the NSE varies from 0.78 to 0.96. However, it can be seen from the comparison that the performance of the DSL site is worsened than other sites, especially in terms of RMSE. Combined with the detailed information of each site in Table 1, we know that the elevation of the DSL site is the largest among the four sites, reaching 3739 m, followed by 3033 m of the AR site.

On the other hand, two sites, ZY and SDQ, with lower elevations, perform well with the RMSE of 3.92 K and

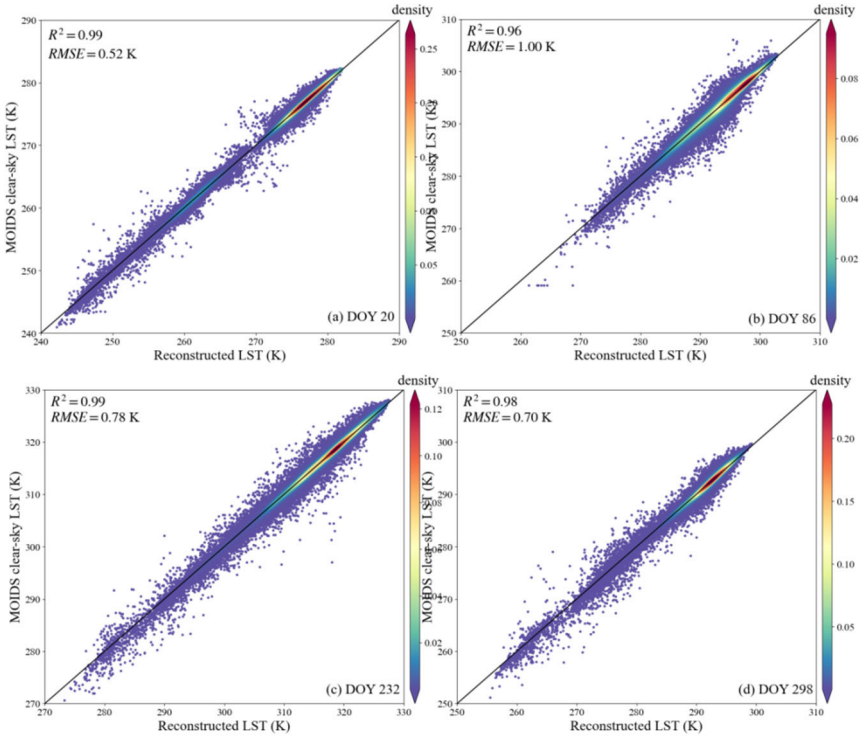

FIGURE 7. Comparison of MODIS clear-sky LST and LST reconstructed by RF in 2019 (DOY 20, DOY 86, DOY 232, and DOY 298).

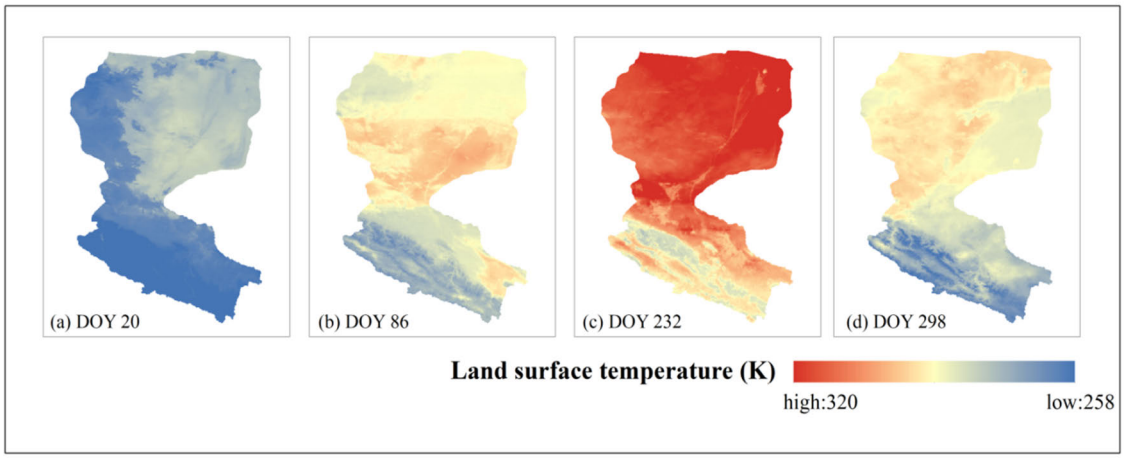

FIGURE 8. Spatial distribution of LST reconstructed by RF in 2019 (DOY 20, DOY 86, DOY 232, and DOY 298).

TABLE 3. The average characteristic importance scores on the reconstructed days.

Characteristic variables	V_{NDVI}	V_{EVI}	V_{MNDWI}	V_{LSWI}	V_{ELV}	V_{SLP}	V_{LAT}	V_{SOL}
Average score	0.08	0.06	0.17	0.19	0.35	0.05	0.19	0.06

4.38 K, respectively. Although the factor of elevation was considered and used as the characteristic variable of LST to participate in the training of the random forest model, it also inevitably affected the reconstruction process of LST. However, compared with other LST reconstruction schemes that do not consider elevation, although some sites show a significant deviation, the overall results still show that the reconstructed LST strongly correlates with in situ LST.

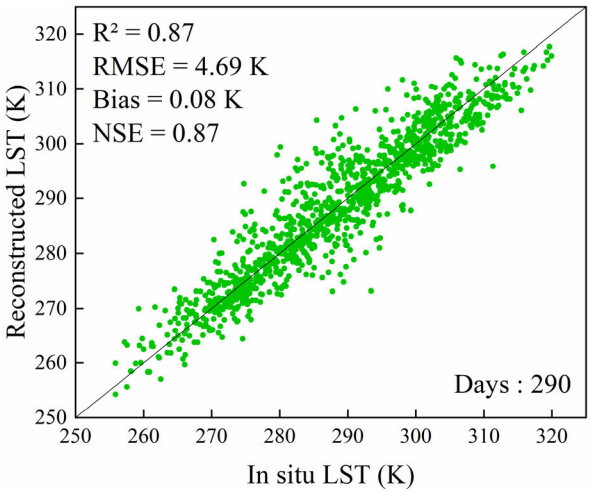

FIGURE 9. Validation of LST reconstructed by the RF model versus LST from AWS observations.

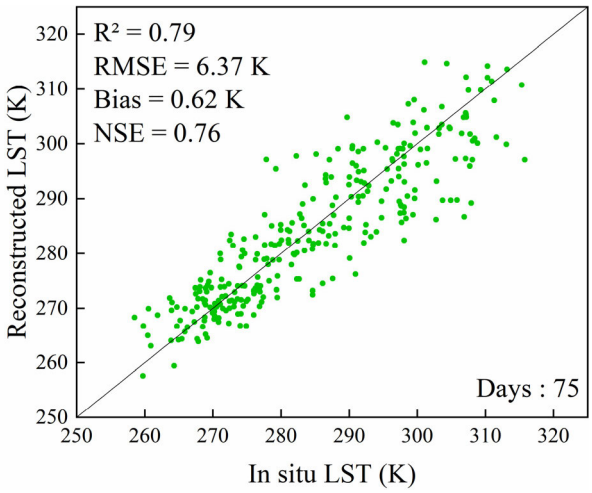

FIGURE 10. Validation of LST reconstructed by using the RF model combined with SP method versus LST from AWS observation.

TABLE 4. The general performance results of LST were reconstructed by using the RF model at four sites.

Sites	R^2	RMSE (K)	Bias (K)	NSE
ZY	0.88	3.92	0.40	0.88
AR	0.80	5.05	0.36	0.82
DSL	0.79	5.26	0.91	0.78
SDQ	0.92	4.38	1.34	0.96
Overall	0.87	4.69	0.08	0.87

Therefore, we can conclude that the LST reconstruction method based on the random forest model can effectively recover the invalid LST pixels under the cloud.

2) VALIDATION OF RECONSTRUCTION RESULTS THAT DO NOT MEET THE THRESHOLD

In 2019, 75 images did not meet the threshold, and these images that did not meet the threshold were reconstructed using the RF model combined with the SP method. Fig. 10 shows the validation statistics chart of reconstruction results. The R^2, RMSE, Bias, and NSE are 0.79, 6.37 K, 0.62 K, and 0.76, respectively. Compared with Fig. 9, most points are not concentrated near the 1:1 line and appear relatively scattered. Among them, the R^2 (0.79 vs. 0.87), Bias (0.62 K vs. 0.08 K), and NSE (0.76 vs. 0.87) is slightly lower than that of the method directly using the RF model, but the RMSE (6.37 K vs. 4.69 K) has a significant increase. Although this method does not perform as well as the method directly using the random forest model, from the overall reconstruction effect, the evaluation indicators of this method remain within a relatively reasonable range. This method is an effective method for recovering invalid pixels for images with severe cloud pollution and a limited number of clear-sky pixels during LST reconstruction. NSE close to 1 also shows that the reconstruction effect of this method can reach a relatively satisfactory level.

Therefore, we combine two methods to complete the reconstruction of images that meet the threshold and those that do not achieve the reconstruction of the daily gap-free MODIS/Terra LST product. Fig. 11 compares daily reconstructed LST and in situ LST at four sites. Overall, the trend of the reconstructed LST and in situ LST have strong consistency. The NSE of these sites is above 0.76. The two curves show good correlation and similar changes, indicating that the LST reconstruction scheme used in this study can effectively reconstruct the cloud-cover LST. For each site, the DSL site with the highest altitude still performs the worst, with the highest RMSE of 5.57 K, followed by the AR site with an RMSE of 5.20 K. On the other hand, the ZY site and the SDQ site with lower elevations perform better, with the RMSE of 4.87 K and 4.73 K, respectively. Therefore, in the subsequent LST reconstruction process, to obtain a better reconstruction effect, the elevation factor is still worth discussing, especially in areas with complex terrain.

V. DISCUSSIONS

In previous studies, although many machine learning algorithms have been developed for conducting research on LST reconstruction. But most machine learning algorithms often require a large number of training datasets to obtain accurate results. For daily LST images, machine learning can reconstruct images with a large number of clear sky pixels on a certain day. Once there is a high amount of cloud cover or other conditions on a certain day that result in a low number of clear sky pixels, the reconstruction effect of machine learning will be poor, and the reconstruction results are often not continuous. Therefore, the RF model proposed in this article can effectively solve this problem. On the one hand, utilizing the fast and simple advantages of random forest models to complete reconstruction, and on the other hand, using similar pixel methods to supplement the number of training sets. From this, daily gap-free LST data can be

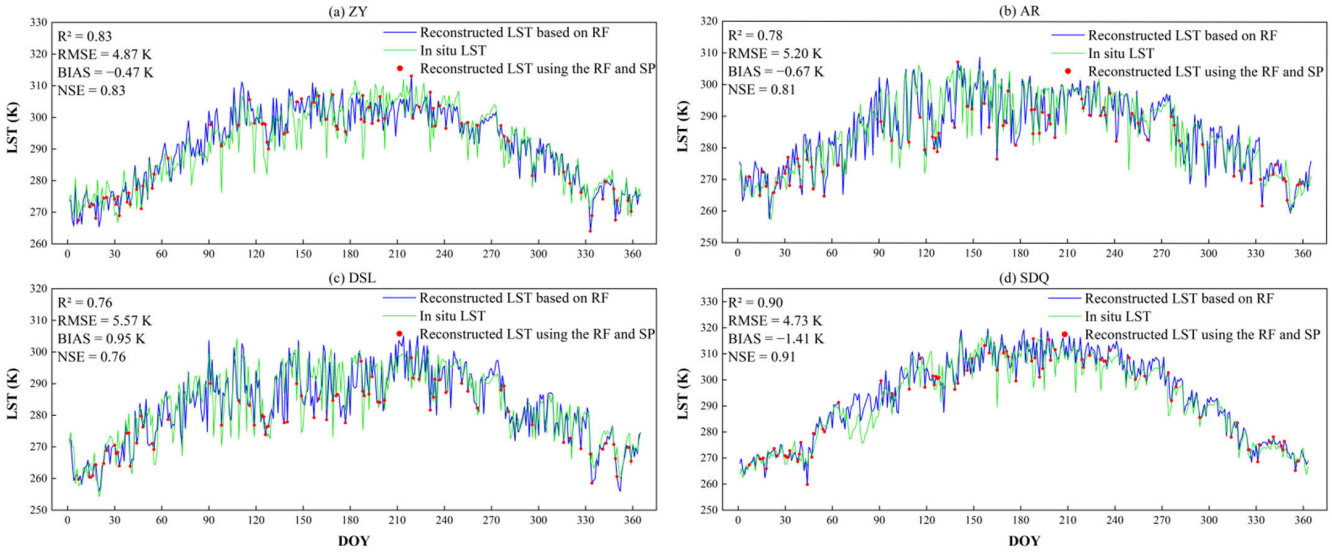

FIGURE 11. Validation of daily LST reconstructed by using the LST reconstruction scheme in this study versus LST from AWS observation.

obtained. Continuous LST dataset is also more valuable for related surface research and other thermal infrared remote sensing studies.

This paper reconstructed the daily MODIS/Terra LST product using the random forest model and similar pixels method. First, the 290 images that meet the threshold were reconstructed by the RF model for the reconstruction process. From the validation results in Fig. 9, the LST reconstructed using the RF model is highly correlated with the in situ LST, which indicates that the RF model is feasible in LST reconstruction. To explore the difference in the reconstruction effect of the RF model in different seasons and the correlation between reconstructed LST and origin LST, we chose four days to represent the four seasons and showed the reconstruction effect. According to the validation indicators in Fig. 7, the RF model maintains relative stability in different seasons. As a machine learning algorithm, the sensitivity of the RF model to the amount of training data has always been a concern. Comparing the number of training sets and reconstruction accuracy in these four days, we can find that the reconstruction accuracy was also increasing with the data volume increase. This is consistent with most studies [52], [53]. R^2 increased from 0.96 to 0.99, and RMSE decreased from 1 k to 0.52 K. But as the day with the most training data set, the RMSE of DOY 232 is not the lowest with 0.78 K. Because RMSE is still sensitive to some outliers even though the data volume is large.

Nevertheless, the RMSE of 0.78 K is still within a reasonable range. Generally speaking, when the data quality meets the requirements, the larger the data volume, the richer the data features that the RF model can extract, and the better the reconstruction accuracy. However, the validation indicators will not change significantly. The RF model can calculate the importance of the independent variable according to the change of error. The importance is an indicator to quantitatively evaluate the impact of each influence factor on the surface temperature—the greater the importance value, the greater the impact on the surface temperature reconstruction [46]. Table 2 shows the average importance scores in the reconstruction process using the RF model. V_{ELV} has the highest score, with 0.35, which indicates that elevation is the most critical factor affecting LST. Some previous researchers chose elevation over all other LST-related variables. This is because the elevation is a measurable variable linked to LST [29], [54], [55]. Mushore et al. [56] and Sun et al. [57] all obtained an inverse relationship between the LST and the elevation, namely that the higher the elevation, the weaker the correlation between the LST reconstruction accuracy and the elevation. Subsequent validation results further proved this point. The reconstruction effect of the two sites with high elevation (AR and DSL) is worsened than those with low elevation (ZY and SDQ). This may be due to the complex terrain and elevation differences caused by different slope effects, affecting the amount of radiation received by the surface and the elevation of the air temperature regulation effect. According to Fig. 1 and Table 1, the Heihe River Basin is a region with complex terrain and colossal elevation difference. The elevation difference between the lowest and highest points can reach more than 4000 meters. Therefore, elevation is a vital factor that this study cannot ignore. In addition, V_{LAT} also played an essential role in the reconstruction process, with a score of 0.19. For the Heihe River Basin, a region that spans three provinces and has a substantial north-south span, the regulation effect of latitude is still pronounced. In future research, we will further explore the influence of relevant characteristic variables on the reconstruction accuracy and carry out different algorithms to optimize the reconstruction model, especially the influence of elevation.

Second, the 75 images that did not meet the threshold were reconstructed using the RF model and SP method. It is infeasible to directly use the RF model for those images with severe cloud pollution and almost no clear-sky pixels. Therefore, we consider the temporal-related information and train together with the clear-sky pixels in the neighborhood and their clear-sky pixels to complete the reconstruction of these images. According to Fig. 10, the reconstruction effect of this method is not as good as that of using the RF model directly. Because of these images with severe cloud pollution, the available adequate information is minimal. Even if adequate information in the temporal domain is combined, it is not directly related to them. Therefore, the effect of image reconstruction using the information directly related to itself is better than this method. In addition, the amount of available data is less due to the severe cloud and fog, and the size of the data volume also affects the accuracy of reconstruction to a certain extent. But overall, the reconstruction accuracy using this method is still satisfactory. Although the RMSE is relatively large, the overall R^2 and NSE reach 0.79 and 0.76, respectively. Finally, we combined the two methods to analyze the daily reconstruction results. The results in Fig. 11 show that the two curves have high coincidence and similar change trends. Validation indicators show that the reconstructed LST strongly correlates with in situ LST. Therefore, the RF-based LST reconstruction scheme proposed in this study can effectively restore the land surface temperature under cloud condition.

VI. CONCLUSION

Land surface temperature (LST) is a vital indicator of energy partitioning at the land surface-atmosphere boundary and is sensitive to changing surface conditions. Satellite remote sensing provides opportunities to estimate global and continuous LSTs. It is widely used in earth resources, environment, attitude systems, hydrology, etc. However, remote sensing data are inevitably affected by clouds. Under cloudy conditions, LST products will have many observation gaps, reducing their accuracy, which significantly limits the broad application of LST products. Therefore, recovering invalid values is a crucial challenge for LST product application and is significant.

In recent years, machine learning algorithms have provided new technical means for the seamless observation of land surface temperature. Based on the algorithm of random forest in machine learning, this paper reconstructed the missing pixels in the Heihe River Basin's MODIS/Terra LST product in 2019. We set a threshold for the daily MODIS/Terra LST product quality and divided the images with the clear-sky pixels percentage greater than 30% (290 images) and those with clear-sky pixels less than 30% (75 images) into one group, respectively. First, we used the RF model to train images that met the threshold and introduced some characteristic variables related to LST into the RF model. The visual assessment indicated that the reconstructed LST image could fully capture the spatial distribution features of LST related-characteristics variables. The reconstructed LST had a strong correlation with the original LST, with all R^2 significant than 0.96 and all RMSE less than 1 K. From the overall validation results of the four sites, the R^2 and NSE reached 0.87 and 0.87, respectively. The RMSE and the Bias reached 4.69 K and 0.08 K, respectively. This showed that the RF model performed well reconstructing LST. Through the analysis of the characteristic importance score, we found that elevation is the most crucial factor affecting LST reconstruction, with a score of 0.35, followed by LSWI and latitude. Second, we used the RF model and SP method to recover invalid values for images that do not meet the threshold. For each image that does not meet the threshold value, we can find an image close to and meets the threshold value in the time series. The clear-sky pixels of the two images were combined and put into the RF model to recover the invalid values. From the reconstruction effect, the overall reconstruction accuracy can reach a satisfactory level with an R^2 of 0.79, an NSE of 0.76, and an RMSE and Bias of 6.37 K and 0.62 K, respectively. We completed the daily MODIS/Terra LST product reconstruction through the above two methods. From the validation indicators of the four sites, the reconstructed LST had a strong correlation with the in situ LST.

In this study, we generated daily MODIS/Terra LST product using the RF model and SP method. Our RF-based LST reconstruction scheme can accurately restore invalid LST pixels based on the validation results. It provides a theoretical reference for the accurate acquisition of surface temperature reconstruction results based on the machine learning method. It brings a new idea for MODIS LST products reconstruction in the Heihe River Basin and other regions.

ACKNOWLEDGMENT

The authors would like to thank the National Tibetan Plateau Data Center (http://data.tpdc.ac.cn (accessed from January to July 2022)) for providing the AWS measurements and solar radiation data. They also thank NASA and USGS for providing the MODIS products.

REFERENCES

[1] D. Li and L. Wang, "Sensitivity of surface temperature to land use and land cover change-induced biophysical changes: The scale issue," *Geophys. Res. Lett.*, vol. 46, no. 16, pp. 9678–9689, Aug. 2019.

[2] Z.-L. Li, B.-H. Tang, H. Wu, H. Ren, G. Yan, Z. Wan, I. F. Trigo, and J. A. Sobrino, "Satellite-derived land surface temperature: Current status and perspectives," *Remote Sens. Environ.*, vol. 131, pp. 14–37, Apr. 2013.

[3] P. J. Sellers, F. G. Hall, G. Asrar, D. E. Strebel, and R. E. Murphy, "The first ISLSCP field experiment (FIFE)," *Bull. Amer. Meteorological Soc.*, vol. 69, no. 1, pp. 22–27, Jan. 1988.

[4] S. Liang, "An optimization algorithm for separating land surface temperature and emissivity from multispectral thermal infrared imagery," *IEEE Trans. Geosci. Remote Sens.*, vol. 39, no. 2, pp. 264–274, Feb. 2001.

[5] D. J. Mildrexler, M. Zhao, W. B. Cohen, S. W. Running, X. P. Song, and M. O. Jones, "Thermal anomalies detect critical global land surface changes," *J. Appl. Meteorol. Climatol.*, vol. 57, no. 2, pp. 391–411, Feb. 2018.

[6] Y. Xu, A. Knudby, Y. Shen, and Y. Liu, "Mapping monthly air temperature in the Tibetan Plateau from MODIS data based on machine learning methods," *IEEE J. Sel. Topics Appl. Earth Observ. Remote Sens.*, vol. 11, no. 2, pp. 345–354, Feb. 2018.

[7] Z.-L. Li, H. Wu, N. Wang, S. Qiu, J. A. Sobrino, Z. Wan, B.-H. Tang, and G. Yan, "Land surface emissivity retrieval from satellite data," *Int. J. Remote Sens.*, vol. 34, nos. 9–10, pp. 3084–3127, May 2013.

[8] Q. Tong, Y. Xue, and L. Zhang, "Progress in hyperspectral remote sensing science and technology in China over the past three decades," *IEEE J. Sel. Topics Appl. Earth Observ. Remote Sens.*, vol. 7, no. 1, pp. 70–91, Jan. 2014.

[9] L. M. Mcmillin, "Estimation of sea surface temperatures from two infrared window measurements with different absorption," *J. Geophys. Res.*, vol. 80, no. 36, pp. 5113–5117, Dec. 1975.

[10] S. M. Alfieri, F. De Lorenzi, and M. Menenti, "Mapping air temperature using time series analysis of LST: The SINTESI approach," *Nonlinear Processes Geophys.*, vol. 20, no. 4, pp. 513–527, Jul. 2013.

[11] D. Long, L. Yan, L. Bai, C. Zhang, X. Li, H. Lei, H. Yang, F. Tian, C. Zeng, X. Meng, and C. Shi, "Generation of MODIS-like land surface temperatures under all-weather conditions based on a data fusion approach," *Remote Sens. Environ.*, vol. 246, Sep. 2020, Art. no. 111863.

[12] S. Duan, Z. Li, H. Li, F. M. Göttsche, H. Wu, W. Zhao, and C. Coll, "Validation of collection 6 MODIS land surface temperature product using in situ measurements," *Remote Sens. Environ.*, vol. 225, pp. 16–29, May 2019.

[13] Y. Jiang, R. Tang, X. Jiang, Z. Li, and C. Gao, "Estimation of soil evaporation and vegetation transpiration using two trapezoidal models from MODIS data," *J. Geophys. Res., D. Atmos.*, vol. 124, no. 14, pp. 7647–7664, 2019.

[14] P. Fu and Q. Weng, "Variability in annual temperature cycle in the urban areas of the United States as revealed by MODIS imagery," *ISPRS J. Photogramm. Remote Sens.*, vol. 146, pp. 65–73, Dec. 2018.

[15] C. Zeng, H. Shen, M. Zhong, L. Zhang, and P. Wu, "Reconstructing MODIS LST based on multitemporal classification and robust regression," *IEEE Geosci. Remote Sens. Lett.*, vol. 12, no. 3, pp. 512–516, Mar. 2015.

[16] W. Yu, M. Ma, X. Wang, and J. Tan, "Estimating the land-surface temperature of pixels covered by clouds in MODIS products," *J. Appl. Remote Sens.*, vol. 8, no. 1, Nov. 2014, Art. no. 083525.

[17] M. Metz, D. Rocchini, and M. Neteler, "Surface temperatures at the continental scale: Tracking changes with remote sensing at unprecedented detail," *Remote Sens.*, vol. 6, no. 5, pp. 3822–3840, Apr. 2014.

[18] M. Jin, "Interpolation of surface radiative temperature measured from polar orbiting satellites to a diurnal cycle: 2. Cloudy-pixel treatment," *J. Geophys. Res., Atmos.*, vol. 105, no. D3, pp. 4061–4076, Feb. 2000.

[19] W. Tan, C. Wei, Y. Lu, and D. Xue, "Reconstruction of all-weather daytime and nighttime MODIS Aqua-terra land surface temperature products using an XGBoost approach," *Remote Sens.*, vol. 13, no. 22, p. 4723, Nov. 2021, doi: 10.3390/rs13224723.

[20] S. W. Lyon, R. Sorensen, J. Stendahl, and J. Seibert, "Using landscape characteristics to define an adjusted distance metric for improving Kriging interpolations," *Int. J. Geogr. Inf. Sci.*, vol. 24, no. 5, pp. 723–740, 2010.

[21] L. Ke, X. Ding, and C. Song, "Reconstruction of time-series MODIS LST in central Qinghai-Tibet Plateau using geostatistical approach," *IEEE Geosci. Remote Sens. Lett.*, vol. 10, no. 6, pp. 1602–1606, Nov. 2013.

[22] M. P. Arroyo, and S. O. Villajos. (2016). *Linear Temporal Interpolation Method in Etm+ Using Modis Data*. [Online]. Available: https://www.rxiv.org/abs/1605.0189

[23] G. Zhang, X. Xiao, J. Dong, W. Kou, C. Jin, Y. Qin, Y. Zhou, J. Wang, M. A. Menarguez, and C. Biradar, "Mapping paddy Rice planting areas through time series analysis of MODIS land surface temperature and vegetation index data," *ISPRS J. Photogramm. Remote Sens.*, vol. 106, pp. 157–171, Aug. 2015.

[24] J. Yan, R. Shen, Y. Bao, and L. I. Xinchuan, "Research on the reconstructing of MODIS LST product of Jiangsu province," *Environ. Technol.*, vol. 37, no. 1, pp. 160–167, Jan. 2014.

[25] G. Yang, W. Sun, H. Shen, X. Meng, and J. Li, "An integrated method for reconstructing daily MODIS land surface temperature data," *IEEE J. Sel. Topics Appl. Earth Observ. Remote Sens.*, vol. 12, no. 3, pp. 1026–1040, Mar. 2019.

[26] Y. Chen, Z. Nan, S. Zhao, and Y. Xu, "A Bayesian approach for interpolating clear-sky MODIS land surface temperatures on areas with extensive missing data," *IEEE J. Sel. Topics Appl. Earth Observ. Remote Sens.*, vol. 14, pp. 515–528, Nov. 2021.

[27] W. Yu, Z. Nan, Z. Wang, H. Chen, T. Wu, and L. Zhao, "An effective interpolation method for MODIS land surface temperature on the Qinghai–Tibet Plateau," *IEEE J. Sel. Topics Appl. Earth Observ. Remote Sens.*, vol. 8, no. 9, pp. 4539–4550, Sep. 2015.

[28] J. Tan, T. Che, J. Wang, J. Liang, Y. Zhang, and Z. Ren, "Reconstruction of the daily MODIS land surface temperature product using the two-step improved similar pixels method," *Remote Sens.*, vol. 13, no. 9, p. 1671, Apr. 2021.

[29] D. Chen, Q. Zhuang, L. Zhu, and W. Zhang, "Comparison of methods for reconstructing MODIS land surface temperature under cloudy conditions," *Appl. Sci.*, vol. 12, no. 12, p. 6068, Jun. 2022, doi: 10.3390/app12126068.

[30] D. Long, L. Bai, L. Yan, C. Zhang, W. Yang, H. Lei, and C. Shi, "Generation of spatially complete and daily continuous surface soil moisture of high spatial resolution," *Remote Sens. Environ.*, vol. 233, Aug. 2019, Art. no. 111364.

[31] Y. Li, M. Li, C. Li, and Z. Liu, "Forest aboveground biomass estimation using Landsat 8 and Sentinel-1A data with machine learning algorithms," *Sci. Rep.*, vol. 10, no. 1, p. 9952, Jun. 2020.

[32] Z. Wu, H. Teng, H. Chen, L. Han, and L. Chen, "Reconstruction of gap-free land surface temperature at a 100 m spatial resolution from multidimensional data: A case in Wuhan, China," *Sensors*, vol. 23, no. 2, p. 913, Jan. 2023, doi: 10.3390/s23020913.

[33] Y. Liu, S. Ortega-Farías, F. Tian, S. Wang, and S. Li, "Estimation of surface and near-surface air temperatures in arid Northwest China using Landsat satellite images," *Frontiers Environ. Sci*, vol. 9, Dec. 2021, Art. no. 791336.

[34] U. Khalil, U. Azam, B. Aslam, I. Ullah, A. Tariq, Q. Li, and L. Lu, "Developing a spatiotemporal model to forecast land surface temperature: A way forward for better town planning," *Sustainability*, vol. 14, no. 19, p. 11873, Sep. 2022.

[35] J. Chung, Y. Lee, W. Jang, S. Lee, and S. Kim, "Correlation analysis between air temperature and MODIS land surface temperature and prediction of air temperature using TensorFlow long short-term memory for the period of occurrence of cold and heat waves," *Remote Sens.*, vol. 12, no. 19, p. 3231, Oct. 2020.

[36] D. Yang, S. Zhong, X. Mei, X. Ye, F. Niu, and W. Zhong, "A comparative study of several popular models for near-land surface air temperature estimation," *Remote Sens.*, vol. 15, no. 4, p. 1136, Feb. 2023.

[37] J. Che, M. Ding, Q. Zhang, Y. Wang, W. Sun, Y. Wang, L. Wang, and B. Huai, "Reconstruction of near-surface air temperature over the Greenland ice sheet based on MODIS data and machine learning approaches," *Remote Sens.*, vol. 14, no. 22, p. 5775, Nov. 2022.

[38] H. R. Shwetha and D. N. Kumar, "Prediction of high spatio-temporal resolution land surface temperature under cloudy conditions using microwave vegetation index and ANN," *ISPRS J. Photogramm. Remote Sens.*, vol. 117, pp. 40–55, Jul. 2016.

[39] R. Wang, X. You, Y. Shi, C. Yong, and B. Liu, "Study on air temperature estimation and its influencing factors in a complex mountainous area," *PLoS ONE*, vol. 17, Aug. 2022, Art. no. e0272946.

[40] M. Sahin, "Modelling of air temperature using remote sensing and artificial neural network in Turkey," *Adv. Space Res.*, vol. 50, no. 7, pp. 973–985, Oct. 2012.

[41] P. Wu, Z. Yin, H. Yang, Y. Wu, and X. Ma, "Reconstructing geostationary satellite land surface temperature imagery based on a multiscale feature connected convolutional neural network," *Remote Sens.*, vol. 11, no. 3, p. 300, Feb. 2019.

[42] H. Wu and W. Ying, "Benchmarking machine learning algorithms for instantaneous net surface shortwave radiation retrieval using remote sensing data," *Remote Sens.*, vol. 11, no. 21, p. 2520, Oct. 2019.

[43] W. Zhao and S.-B. Duan, "Reconstruction of daytime land surface temperatures under cloud-covered conditions using integrated MODIS/terra land products and MSG geostationary satellite data," *Remote Sens. Environ.*, vol. 247, Sep. 2020, Art. no. 111931.

[44] W. Li, L. Ni, Z.-L. Li, S.-B. Duan, and H. Wu, "Evaluation of machine learning algorithms in spatial downscaling of MODIS land surface temperature," *IEEE J. Sel. Topics Appl. Earth Observ. Remote Sens.*, vol. 12, no. 7, pp. 2299–2307, Jul. 2019.

[45] Y. Yang, C. Cao, X. Pan, X. Li, and X. Zhu, "Downscaling land surface temperature in an arid area by using multiple remote sensing indices with random forest regression," *Remote Sens.*, vol. 9, no. 8, p. 789, Jul. 2017.

[46] Y. Xiao, W. Zhao, M. Ma, and K. He, "Gap-free LST generation for MODIS/terra LST product using a random forest-based reconstruction method," *Remote Sens.*, vol. 13, no. 14, p. 2828, Jul. 2021.

[47] S. M. Liu, Z. W. Xu, W. Z. Wang, Z. Z. Jia, M. J. Zhu, J. Bai, and J. M. Wang, "A comparison of eddy-covariance and large aperture scintillometer measurements with respect to the energy balance closure problem," *Hydrol. Earth Syst. Sci.*, vol. 15, no. 4, pp. 1291–1306, Apr. 2011.
[48] S. Liu, X. Li, Z. Xu, T. Che, Q. Xiao, M. Ma, and Z. Ren, "The Heihe integrated observatory network: A basin-scale land surface processes observatory in China," *Vadose Zone J.*, vol. 17, no. 1, pp. 1–12, Dec. 2018.
[49] L. Husi, T. Wang, and Y. Du. (2021). *East Asia–Pacific Longwave/Shortwave Downward Radiation at the Surface Data Set (2016-2020)*. [Online]. Available: https://doi.org/10.11888/Meteoro.tpdc.271729
[50] A. Mokhtari, H. Noory, F. Pourshakouri, P. Haghighatmehr, Y. Afrasiabian, M. Razavi, F. Fereydooni, and A. S. Naeni, "Calculating potential evapotranspiration and single crop coefficient based on energy balance equation using Landsat 8 and Sentine1–2," *ISPRS-J. Photogramm. Remote Sens.*, vol. 154, pp. 231–245, Aug. 2019.
[51] K. Gu, Y. Zhang, and J. Qiao, "Random forest ensemble for river turbidity measurement from space remote sensing data," *IEEE Trans. Instrum. Meas.*, vol. 69, no. 11, pp. 9028–9036, Nov. 2020.
[52] M. Belgiu and L. Drăguţ, "Random forest in remote sensing: A review of applications and future directions," *ISPRS J. Photogramm. Remote Sens.*, vol. 114, pp. 24–31, Apr. 2016.
[53] R. Taormina and K. W. Chau, "ANN-based interval forecasting of streamflow discharges using the LUBE method and MOFIPS," *Eng. Appl. Artif. Intell.*, vol. 45, pp. 429–440, Oct. 2015.
[54] L. Ke, Z. Wang, C. Song, and Z. Lu, "Reconstruction of MODIS LST time series and comparison with land surface temperature (T) among observation stations in the northeast Qinghai-Tibet Plateau," *Prog. Geography*, vol. 2, no. 1, pp. 819–826, 2011.
[55] M. Neteler, "Estimating daily land surface temperatures in mountainous environments by reconstructed MODIS LST data," *Remote Sens.*, vol. 2, no. 1, pp. 333–351, Jan. 2010.
[56] T. D. Mushore, O. Mutanga, and J. Odindi, "Estimating urban LST using multiple remotely sensed spectral indices and elevation retrievals," *Sustain. Cities Soc.*, vol. 78, Mar. 2022, Art. no. 103623.
[57] Q. Sun, Z. Wu, and J. Tan, "The relationship between land surface temperature and land use/land cover in Guangzhou, China," *Environ. Earth Sci.*, vol. 65, no. 6, pp. 1687–1694, Mar. 2012.

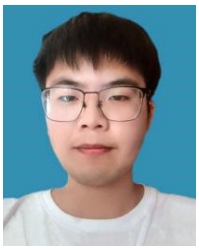

DONG CHEN was born in Huai'an, Jinagsu, China. He received the B.S. degree in surveying engineering from the North China University of Science and Technology, Tangshan, China, in 2019. He is currently pursuing the M.S. degree in civil engineering and water resources with Nanjing Tech University.

His current research interests include thermal infrared remote sensing and machine learning.

QIFENG ZHUANG was born in Yixing, Jiangsu, China, in 1988. He received the B.S. degree from Nanjing Normal University, in 2011, and the Ph.D. degree in geographic information science from the Institute of Remote Sensing and Digital Earth, Chinese Academy of Sciences, in 2016.

Since 2017, he has been a Lecturer with the College of Geomatics Science and Technology, Nanjing Tech University, China. His current research interests include the remote sensing of agriculture and water resources.

LIANG ZHU was born in Honghu, Hubei, China, in 1982. He received the Ph.D. degree in cartography and geographical information systems from the Institute of Remote Sensing Application, Chinese Academy of Sciences, in 2009.

He is currently an Assistant Professor with the State Key Laboratory of Remote Sensing Science, Aerospace Information Research Institute, Chinese Academy of Sciences. His current research interests include remote sensing-based agriculture monitoring and LUCC.

WENJIE ZHANG was born in Suzhou, Anhui, China, in 1997. He received the B.S. degree in geographic information science from Nanjing Tech University, in 2021, where he is currently pursuing the M.S. degree.

His current research interests include remote sensing resources for agriculture and water resources.

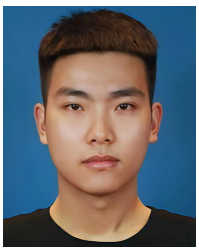

TAO SUN was born in Qingdao, Shandong, China, in 2000. He received the B.S. degree in surveying engineering from Shandong Agricultural and Engineering University, in 2022. He is currently pursuing the M.S. degree with Nanjing Tech University.

His current research interests include data downscaling and remote sensing image processing.